Three-dimensional Monte Carlo simulation of nanorod self-organization in REBa$_2$Cu$_3$O$_y$ thin films grown by vapor phase epitaxy

Yusuke Ichino*, Yutaka Yoshida, and Shun Miura

Department of Energy Engineering and Science, Nagoya University, Nagoya 464-8603, Japan

*E-mail: ichino@nuee.nagoya-u.ac.jp

Some metal-complex oxides (MCOs) self-organize within REBa$_2$Cu$_3$O$_y$ (REBCO: RE=rare earth) superconducting thin films grown by vapor phase epitaxy. To clarify the self-organization mechanism, we developed a three-dimensional Monte Carlo (3D-MC) simulation code using a simple model and simulated nanorod growth under various growth conditions. As a result, the self-organization of nanorods was reproduced by 3D-MC simulations and we clarified the nanorod growth mechanism as follows. The growth mode of MCO particles was 3D island growth due to the instability of the interface of the MCO and the substrate. On the other hand, that of REBCO particles was 2D island growth. There were diverse nanostructures, which were strongly affected by substrate temperature (T_s) and deposition rate (v_{dep}). We constructed a contour plot of the nanorod number density and a phase diagram of the nanostructures depending on T_s and v_{dep}.

1. Introduction

$REBa_2Cu_3O_y$ (REBCO, RE=Y and rare-earth) superconductors show excellent superconducting properties such as critical current density (J_c) in magnetic fields. Some groups have reported the self-organization of $BaZrO_3$ (BZO) within REBCO films grown by vapor phase epitaxy[1] and that BZO forms many nanorods threading the films[2,3]. This self-organization into nanorods is also confirmed in other metal-complex oxides (MCOs), for example, $BaMO_3$ (BMO; M= Sn and Hf)[4-9], $Ba(RE,Nb)O_3$ double perovskite[10-17], and rare-earth tantalate pyrochlore[18]. These nanorods contribute to the enhancement of J_c in magnetic fields, since they act as strong flux pinning centers within REBCO films. Among these MCOs, $BaHfO_3$ (BHO) attracts considerable attention because REBCO films including BHO nanorods, which are prepared by pulsed laser deposition (PLD) method, show markedly high J_c values in magnetic fields compared with non-doped and other BMO-doped REBCO films[8,19-24]. J_c in magnetic fields is determined by the flux pinning force of nanorod characteristics such as diameter and number density. The characteristics can be controlled by growth conditions such as growth temperature. We prepared a 4.1 vol% BHO-doped $SmBa_2Cu_3O_y$ (SmBCO) thin film at a low substrate temperature of 1,023 K (750ºC) and confirmed that BHO nanorods of small diameter and high number density were included in the SmBCO films[20]. Their number density was 2,830 /μm^2 and their average diameter was 7.0 nm. In the case of a 3.7 vol% BHO-doped film prepared by conventional PLD method at a substrate temperature of 1,213 K (940ºC)[19], the number density and average diameter were 708 /μm^2 and 13.5 nm, respectively. Recently, we have reported an excellent flux pinning force of 1.6 TN/m^3 at 4.2 K in a BHO-doped SmBCO film deposited at a relatively low growth temperature of 993 K (720ºC)[23]. Other MCO nanorods are also affected by deposition conditions. For

example, $BaNb_2O_6$ (BNO)-doped ErBCO films included many nanorods composed of $Ba(Er,Nb)O_3$ (BENO)[11,14]. With increasing substrate temperature, the diameter of BENO nanorods increased; however, the number density decreased. These tendencies are the same as those of our BHO-doped SmBCO films. Haruta et al. prepared $BaNb_2O_6$-doped ErBCO and YBCO films by Nd:YAG-PLD method, which had many nanorods[24]. They investigated the substrate temperature dependence of nanorod configurations, such as the length and tilt angle of the nanorods, and found that the configurations depended on the substrate temperature. Maiorov et al. reported that nanostructures in BZO-doped YBCO films can be controlled by adjusting the substrate temperature and deposition rate[25]. From these experimental findings, one can see that the self-organization of MCO nanorods is affected by deposition conditions such as substrate temperature and deposition rate.

This self-organization has also been similarly observed in multiferroic films that have two components: $CoFe_2O_4$ and $BiFeO_3$[26] and also $CoFe_2O_4$ and $PbTiO_3$[27]. In these films, structures similar to nanorods, which were called "nanopillars", were observed and the authors explained that the difference in wettability between the film material and the nanorod material on the substrate resulted in the formation of nanorods.

Control of nanorod morphologies is important for the control of the superconducting properties of the MCO-doped REBCO films. Wu et al. examined BZO nanorods self-organization in YBCO films using an elastic strain model[28]. They described that an increase in BZO doping concentration led to an increase in nanorod density; thus, the matching field increased. In order to clarify the self-organization mechanism, the numerical simulation of thin film crystal growth is one of the useful methods. The Monte Carlo (MC) simulation has been widely adopted to the study of thin film crystal growth.

In the case of REBCO thin film growth, Tretiatchenko successfully reproduced the complicated transformation of the surface morphology of the REBCO films[29]. He took into account preferentially oriented grains depending on the growth temperature. Zheng et al. used cross-sectional two-dimensional (2D) MC simulations to study the kinetic effects on the morphological evolution of a two-component epitaxial system[30]. They elucidated that column-like nanostructures were only formed when the bond energy between different atoms on the growth surface was much lower than that between the same atoms. We developed 2D MC simulations for an initial growth stage on a substrate surface of a two-component system[31]. We simulated self-organization on the substrate surface and found that the number density of nanorods decreased with increasing growth temperature. However, the self-organization process of nanorods or other nanostructures depending on growth conditions such as temperature and deposition rate has not yet been clarified in detail.

On the basis of the above, we aim to clarify the self-organization mechanism in REBCO thin films with BMO. In this study, we develop a three-dimensional (3D) MC simulation for the thin film growth of a two-component system and try to reproduce the self-organization of nanostructures. Additionally, we examine the effects of substrate temperature and deposition rate on self-organization characteristics such as number density and morphologies.

2. Simulation methods

We used a simple 3D-MC model as follows. REBCO and BMO unit cells are expressed using simple cubes with one side indicated by $a = 0.4$ nm, as shown in Fig. 1(a). We present a REBCO unit cell as an A particle, which consists of three cubes, and

4

a BMO unit cell as a B particle, which includes only one cube, in this paper.   We assume

that the substrate is made of A particles, and this assumption considers that the substrate

is a single crystal of an A particle.   The particles are adsorbed on the substrate from the

vapor phase, namely, we consider a physical vapor deposition process.   The adsorbed

particles can occupy positions in the sites of the substrate.   There are no chemical

reactions on the surface, and the A and B particles do not react with other kinds of particles.

The particles experience randomly chosen events, which are adsorption on the crystal

growth surface, surface diffusion, and desorption from the surface.   The particles are

allowed to move to only the nearest-neighbor site.   Bulk diffusion is not taken into

account in this simulation.   The particles grow with a cube-on-cube in-plane orientation.

The A particles always maintain their stacked structure perpendicular to the substrate

surface, which corresponds to the c-axis orientation in REBCO thin films.   In-plane

rotations of both the A and B particles are also not taken into account.

   We carried out the 3D-MC simulations based on the standard Metropolis algorithm

as follows.   At randomly chosen point of substrate sites during each MC simulation step,

one of the three possible events could randomly occur.   The probabilities of adsorption

(r_{ads}) and surface diffusion (r_{diff}) on a single surface site are denoted by $r_{ads} = Fa^2$ and r_{diff}

$= D/a^2$, respectively.   Here, F and D are the incident flux with a unit of $m^{-2} \cdot s^{-1}$ and the

surface diffusion constant with a unit of m^2/s, respectively.   The growth kinetics are

controlled by the dimensionless ratio (R) of these probabilities, $R = r_{ads} / r_{diff} = Fa^4 / D$.

We can exchange the deposition rate (v_{dep}) of REBCO films with a unit of m/s to F by

using the relation $F = v_{dep}/(3a^3)$. D depends on substrate temperature (T_s).   Dam et al.

estimated D from the surface morphologies of YBCO films depending on the substrate

temperature[32) and we used the reported D values ranging from 10^{-16} to 10^{-15} m^2/s in this

study. When an adsorbed particle randomly diffuses on the surface, we calculate the initial coordination energy (E_i) before the random walk and the final coordination energy (E_f) after the random walk. If E_f is smaller than E_i, the particle preferentially moves to the final state. However, if E_f is larger than E_i, a probability to move to the final state is defined by the Boltzmann distribution of $\exp(-\Delta E /k_B T)$, where ΔE is $E_f - E_i$ and k_B is the Boltzmann constant. A schematic diagram of the coordination energy is presented in Fig. 1(b). The coordination energy is calculated by counting inter-particle bond energies. We describe the bond energy density between A particles as E_{AA}; here, the bond energy density is defined by a bond energy per side face of a cube. Similarly, E_{BB} is the bond energy density between B particles, and E_{AB} is the bond energy density between an A particle and a B particle. We do not consider the anisotropy of the bond energy density and introduce only the nearest-neighbor interaction between the particles. E_{AA} and E_{BB} correspond to the decomposition energies of both materials. For example, the E_{AA} of YBCO could be smaller than that of SmBCO, because the melting temperature (peritectic temperature) of YBCO is lower than that of SmBCO. Similarly, E_{BB} is also related to the decomposition energy of a BMO material. E_{AB} means interfacial instability between REBCO and BMO. A larger lattice mismatch results in an unstable interface, which leads to a low E_{AB}.

   We used the bond energy densities of $E_{AA} = 2,000$ K, $E_{BB} = 2,500$ K, and $E_{AB} = 500$ K. In Fig. 1(b), E_{des} corresponds to the energy difference between an adsorbed particle and a particle in the vapor phase, and we used 50,000 K in the simulations. These energies were selected from preliminary simulations, which roughly reproduced the experimental number density of the BHO nanorods in a BHO-doped SmBCO film prepared by conventional PLD method at a T_s of 1,213 K (940ºC)[19]. In the present study,

we concentrated on clarifying the nanostructural self-organization mechanism. Therefore, the role of these bond energies is not discussed in detail in this paper.

Our 3D-MC simulations were undertaken on 200×200 cubic grids of the substrate corresponding to 80 ×80 nm^2 in physical unit. Periodic boundary conditions were imposed in all the in-plane directions. Although the volume fraction of BMO can be changed by varying the number ratio of the adsorbed particles, we fixed the BMO volume fraction to 3 vol% (8.6 mol%) in order to focus on the effects of T_s and v_{dep} on self-organization.

3. Results and discussion

3.1 Self-organization in the 3D-MC simulations

We performed the numerical simulations at $T_s = 1,113$ K (840ºC) and 1,023 K (750ºC). v_{dep} was fixed at 70 nm/h, which corresponds to the typical deposition rate in our experiments. The simulation results are shown in Fig. 2. Here, *A* particles are shown transparent for ease of viewing. One can see that there are many red columns consisting of *B* particles with a diameter of several nanometers. At a high T_s of 1,113 K as shown in Fig. 2(a), there are straight nanorods. On the other hand, many inclined nanorods grow at a low T_s of 1,023 K as shown in Fig. 2(b). These morphologies are roughly the same as those of our previous experimental observations[21]. Previously, we obtained the microstructures of BHO-doped SmBCO films by cross-sectional transmission electron microscopy (TEM). The obtained TEM images showed that BHO nanorods morphologies were affected by T_s, and a high T_s of 1,113 K and a low T_s of 1,023 K led to the growth of straight and inclined nanorods, respectively. Therefore, we successfully reproduced the nanorod self-organization obtained by the 3D-MC simulations.

In order to clarify the mechanism, we show the sequence of the numerical nanorod growth at $T_s = 1{,}113$ K in Fig. 3. The figures in the left column of Fig. 3 are bird's-eye views and those in the right column are cross-sectional views of a single nanorod corresponding to each left figure. One can see the development of nanorod growth with time at a high T_s. From Figs. 3(a) and 3(a'), the crystal growth mode of B particles is 3D island growth mode, which corresponds to the Volwer-Weber type owing to the unstable interface of B particles and the substrate consisting of A particles. After the 3D island emergence, A particles whose growth mode was layer-by-layer or 2D island growth mode covered the substrate surface. Figures 3(b) and (b') show that the 3D island is surrounded by a layer of A particles. Because the 3D island can grow toward any directions, the height of the 3D island increase when the entire substrate surface becomes covered by A particles. Therefore, the height of the 3D island is always larger than that of the layer of A particles, as shown in Figs. 3(c) and 3(c'). These steps are repeated during the vapor phase deposition. Consequently, a straight nanorod of B particles formed in the matrix consisting of A particles [Figs. 3(d) and 3(d')]. This tendency is also experimentally confirmed from the surface morphologies of REBCO films including BMO. In Fig. 4, we show a surface topographic image of a SmBCO film with 3.0 vol% BHO deposited on a LaAlO$_3$ single crystalline substrate by conventional PLD method at $T_s = 870$ºC. There are many bright points, and the number density of the points is comparable to that of BHO nanorods. This image means that the top of the BHO nanorods is higher than the SmBCO layer. This experimental finding agrees with our 3D-MC simulation result as shown in Fig. 3. From the above, it is important to note that the nanorod self-organization is due to the difference in the growth mode of each particle.

In the case of a low T_s of $1{,}023$ K, the growth sequence is shown in Fig. 5. The critical

nucleation radius of nanorods decreases because of the high supersaturation due to the low growth temperature; thus, many nanorods arise and the growth rate of each nanorod decreases. On the other hand, A particles also easily nucleate, and many 2D islands consisting of A particles appear with grains smaller than those at a high T_s. As shown in Figs. 5(a) and 5(a'), the top of a nanorod was not higher than the A particle layer, because the nanorod growth rate was relatively lower than that at a high T_s. The nanorod grew toward only the right, because the left side was covered by the layer of A particles. The right side of the nanorod was also covered by the layer that advanced from the right edge as shown in Figs. 5(b) and 5(b'). During the growth steps, the left side of the nanorod was covered by A particles again [Figs. 5(c) and 5(c')]. These steps were repeated during the deposition, resulting in an inclined nanorod appearing in the matrix, as shown in Figs. 5(d) and 5(d'). Therefore, we conclude that the growth mechanism of inclined nanorods resulted in a similar rate of growth toward the vertical direction of the nanorods and matrix layer.

3.2 Substrate temperature and deposition rate dependences

Nanorod characteristics such as morphologies and number density are affected by many growth conditions. In this section, we discuss the effects of T_s and v_{dep} on nanorod growth.

The T_s dependence of the number density of nanorods is shown in Fig. 6. Experimental data are also plotted and the values are listed in Table I. The simulations are performed in the T_s range from 993 to 1,213 K at an additive B particle amount of 3.0 vol% and a v_{dep} of 70 nm/h, which is the typical deposition rate in our experiments. Experimental data were obtained from our previous reports of BHO-doped SmBCO films

prepared by PLD method and the BHO additive amount was 3 - 4 vol%[19,21-23]. From this figure, the number density decreased with increasing T_s both in the experimental and simulated data. From the basic crystal growth theory, the critical nucleation radius increases with decreasing supersaturation, which decreases with increasing growth temperature. Namely, a high growth temperature leads to a small number density of nuclei. The number density of nanorods depends on the number density of the nuclei of BMO particles, which correspond to the B particles in this study. As a result, the number density of nanorods decreased with increasing T_s as shown in Fig. 6. We can say that our 3D-MC simulation can reproduce the experimental results well. Next, we investigate the v_{dep} effect on nanorod morphologies on the basis of the result.

Figure 7 shows the bird's-eye views of B particle aggregation depending on the v_{dep} range from 10 to 1,000 nm/h. Here, the A particles are shown transparent for ease of viewing. One can see that the nanostructures within the matrix change with v_{dep}. At a low v_{dep} of 10 nm/h, the B particles aggregated into fat and straight nanorods, and their number density was low. As v_{dep} increased, the number density increased and inclined nanorods appeared. At a very high v_{dep} of 1,000 nm/h, the B particles did not aggregate into nanorods sufficiently owing to the low growth rate of nanorods. As a result, numerous short nanorods and nanoparticles were included in the matrix. Maiorov et al. reported that the combination of randomly distributed nanoparticles and nanorods was varied by v_{dep} and T_s during the PLD of BZO-doped YBCO films[32]. The J_c peak with respect to the c-axis in the magnetic field angular dependence of J_c increased with decreasing laser repetition rate owing to the increase in the number of straight nanorods. The laser repetition rate is proportional to the deposition rate. Therefore, the report is consistent with our result in Fig. 7.

We carried out the 3D-MC simulations at various T_s and v_{dep} values. A contour plot of the number density of nanorods and a phase diagram of nanostructures are presented as functions of T_s and v_{dep} in Figs. 8(a) and 8(b), respectively. In Fig. 8(b), we classified morphologies into four types, namely, straight nanorods (NRs), inclined NRs, short NRs + nanoparticles (NPs), and NPs. Here, an inclined NR corresponds to a nanorod that tilted 10º to the substrate surface normal, and we defined a simulation result with more than 50% of inclined NRs to indicate an "inclined NRs morphology". An NP was made of a cluster of B particles with a diameter that is almost the same as its own length along the substrate surface normal. The low T_s and high v_{dep} caused the insufficient growth of nanorods, resulting in numerous nanoparticles in the matrix, as shown in Fig. 8(b). Thus, the number density of nanorods cannot be defined around the top left corner in Fig. 8(a). From Fig. 8(a), the number density increased with increasing v_{dep} and decreasing T_s. Since the volume fraction of B particles corresponding to BMO is constant in this study, the diameter of nanorods decreases with increasing number density. In the case of REBCO-coated conductors, a high deposition rate is required to reduce the production cost. However, if we need straight or inclined nanorods as pinning centers in coated conductors, an extra high deposition rate is not good owing to the insufficient growth of nanorods, and increasing T_s further would be effective for nanorod growth. On the other hand, a low T_s and a high v_{dep} result in very fine nanostructures, such as numerous short nanorods and nanoparticles with small diameters. These fine nanostructures should change the flux pinning landscape. In particular, the flux pinning at a low temperature would be enhanced, and the magnetic field angular dependence of J_c would also be improved because the coherence length of superconductors decreases with decreasing temperature. Therefore, the appropriate size of pinning centers also decreases at a low

measurement temperature.   In fact, we reported that a BHO-doped SmBCO film deposited at a low T_s of 993 K (720℃) showed excellent flux pinning properties at 4.2 K and an isotropic J_c for an applied magnetic field angle, because the film included very fine short nanorods[23].

4. Conclusions

   We developed the 3D-MC simulation code to clarify the self-organization mechanism of BMO nanorod growth in REBCO films, and we reproduced the nanorod growth by 3D-MC simulations.   We found that the nanorods self-organized owing to the difference in the growth mode between BMO and REBCO.   The vertical growth rates of nanorods and the REBCO layer were also important for determining morphologies, such as straight nanorods, inclined nanorods, short nanorods + nanoparticles, and nanoparticles.   These morphologies were affected by substrate temperature and deposition rate during vapor phase deposition.   We constructed the phase diagram of nanostructures depending on substrate temperature and deposition rate.   To obtain straight or inclined nanorods even at a high deposition rate, increasing substrate temperature further would be required.

References

1) J. L. MacManus-Driscoll, S. R. Foltyn, Q. X. Jia, H. Wang, A. Serquis, L. Civale, B. Maiorov, M. E. Hawley, M. P. Maley, and D. E. Peterson, Nat. Mater. **3**, 439 (2004).

2) Y. Yamada, K. Takahashi, H. Kobayashi, M. Konishi, T. Watanabe, A. Ibi, T. Muroga, S. Miyata, T. Kato, T. Hirayama, and Y. Shiohara, Appl. Phys. Lett. **87**, 132502 (2005).

3) S. Kang, A. Goyal, J. Li, A. A. Gapud, P. M. Martin, L. Heatherly, J. R. Thompson, D. K. Christen, F. A. List, M. Paranthaman, and D. F. Lee, Science **311**, 1911 (2006).

4) C. V. Varanasi, P. N. Barnes, J. Burke, L. Brunke, I. Maartense, T. J. Haugan, E. A. Stinzianni, K. A. Dunn, and P. Haldar, Supercond. Sci. Technol. **19**, L37 (2006).

5) J. Hänisch, C. Cai, V. Stehr, R. Hühne, J. Lyubina, K. Nenkov, G. Fuchs, L. Schultz, and B. Holzapfel, Supercond. Sci. Technol. **19**, 534 (2006).

6) M. Namba, S. Awaji, K. Watanabe, S. Ito, E. Aoyagi, H. Kai, M. Mukaida, and R. Kita, Appl. Phys. Express **2**, 073001 (2009).

7) P. Mele, K. Matsumoto, A. Ichinose, M. Mukaida, Y. Yoshida, S. Horii, and R. Kita, Physica C **469**, 1380 (2009).

8) H. Tobita, K. Notoh, K. Higashikawa, M. Inoue, T. Kiss, T. Kato, T. Hirayama, M. Yoshizumi, T. Izumi, and Y. Shiohara, Supercond. Sci. Technol. **25**, 062002 (2012).

9) A. Tsuruta, Y. Yoshida, Y. Ichino, A. Ichinose, K. Matsumoto, and S. Awaji, IEEE Trans. Appl. Supercond. **23**, 8001104 (2013).

10) S. Horii, K. Yamada, H. Kai, A. Ichinose, M. Mukaida, R. Teranishi, R. Kita, K. Matsumoto, Y. Yoshida, J. Shimoyama, and K. Kishio, Supercond. Sci. Technol. **20**, 1115 (2007).

11) H. Kai, S. Horii, A. Ichinose, R. Kita, K. Matsumoto, Y. Yoshida, T. Fujiyoshi, R.

Teranishi, N. Mori, and M. Mukaida, Supercond. Sci. Technol. **23**, 025017 (2010).

12) H. Kai, M. Mukaida, S. Horii, A. Ichinose, R. Kita, S. Kato, K. Matsumoto, Y. Yoshida, R. Teranishi, K. Yamada, and N. Mori, Physica C **463-465**, 895 (2007).

13) K. Yamada, M. Mukaida, H. Kai, R. Teranishi, A. Ichinose, R. Kita, S. Kato, S. Horii, Y. Yoshida, K. Matsumoto, and S. Toh, Appl. Phys. Lett. **92**, 112503 (2008).

14) S. Horii, H. Kai, M. Mukaida, K. Yamada, R. Teranishi, A. Ichinose, K. Matsumoto, Y. Yoshida, R. Kita, J. Shimoyama, and K. Kishio, Appl. Phys. Lett. **93**, 152506 (2008).

15) S. H. Wee, A. Goyal, Y. L. Zuev, C. Cantoni, V. Selvamanickam, and E. D. Specht, Appl. Phys. Express **3**, 023101 (2010).

16) G. Ercolano, S. A. Harrington, H. Wang, C. F. Tsai, and J. L. MacManus-Driscoll, Supercond. Sci. Technol. **23**, 022003 (2010).

17) G. Ercolano, M. Bianchetti, S. C. Wimbush, S. A. Harrington, H. Wang, J. H. Lee, and J. L. MacManus-Driscoll, Supercond. Sci. Technol. **24**, 095012 (2011).

18) S. A. Harrington, J. H. Durrell, B. Maiorov, H. Wang, S. C. Wimbush, A. Kursumovic, J. H. Lee, and J. L. MacManus-Driscoll, Supercond. Sci. Technol. **22**, 022001 (2009).

19) A. Tsuruta, Y. Yoshida, Y. Ichino, A. Ichinose, K. Matsumoto, and S. Awaji, Supercond. Sci. Technol. **27**, 065001 (2014).

20) S. Miura, Y. Yoshida, Y. Ichino, A. Tsuruta, K. Matsumoto, A. Ichinose, and S. Awaji, Jpn. J. Appl. Phys. **53**, 090304 (2014).

21) S. Miura, Y. Yoshida, Y. Ichino, A. Ichinose, K. Matsumoto, and S. Awaji, J. Phys.: Conf. Ser. **507**, 022021 (2014).

22) S. Miura, Y. Yoshida, Y. Ichino, K. Matsumoto, A. Ichinose, and S. Awaji, Supercond. Sci. Technol. **28**, 065013 (2015).

23) S. Miura, Y. Yoshida, Y. Ichino, Q. Xu, K. Matsumoto, A. Ichinose, and S. Awaji, APL Mater. **4**, 016102 (2016).

24) M. Haruta, K. Saura, N. Fujita, Y. Ogura, A. Ichinose, T. Maeda, and S. Horii, Physica C, **494**, 158 (2013).

25) B. Maiorov, S. A. Baily, H. Zhou, O. Ugurlu, J. A. Kennison, P. C. Dowden, T. G. Holesinger, S. R. Foltyn, and L. Civale, Nat. Mater. **8**, 398 (2009).

26) H. Zheng, Q. Zhan, F. Zavaliche, M. Sherburne, F. Straub, M. P. Cruz, L. Q. Chen, U. Dahmen, and R. Ramesh, Nano Lett. **6**, 1401 (2006).

27) Z. Tan, J. Slutsker, and A. L. Roytburd, J. Appl. Phys. **105**, 061615 (2009).

28) J. Z. Wu, J. J. Shi, J. F. Baca, R. Emergo, T. J. Haugan, B. Maiorov, and T. Holesinger, IEEE Trans. Supercond. Sci. Technol. **27**, 044010 (2014).

29) C. G. Tretiatchenko, Physica C **199**, 7 (1992).

30) S. Zheng, W. Zhu, Y. F. Gao, G. M. Stocks, and Z. Zhang, Appl. Phys. Lett. **96**, 071913 (2010).

31) Y. Ichino, A. Tsuruta, S. Miura, Y. Yoshida, M. Yoshizumi, and T. Izumi, IEEE Trans. Appl. Supercond. **25**, 6604506 (2015).

32) B. Dam, J. H. Rector, J. M. Huijbregtse, and R. Griessen, Physica C **305**, 1 (1998).

Figure Captions

Fig. 1. (Color online) Schematic drawings of our simulation model. (a) Events on the substrate surface and (b) energy state diagram of an adsorbed particle depending on the nearest-neighbor particles.

Fig. 2. (Color online) Bird's-eye views of the B particle self-organization in the matrix consisting of A particles. Substrate temperatures of (a) 1,113 and (b) 1,023 K. Here, the A particles are shown transparent for ease of viewing. The volume fraction of B particles is 3.0 vol%.

Fig. 3. (Color online) Snapshots of the growing two-component system with A and B particles at a substrate temperature of 1,113 K and a deposition rate of 70 nm/h. The A and B particles are shown in yellow and red, respectively. The volume fraction of B particles is 3.0 vol%. (a) - (d) are bird's-eye views and (a') - (d') are cross-sectional views corresponding to (a) - (d), respectively.

Fig. 4. (Color online) Surface topographic image of a 3.0 vol% BaHfO$_3$-doped SmBCO film. The film is deposited at a substrate temperature of 1,143 K (870ºC) and a deposition rate of about 100 nm/h by conventional PLD method.

Fig. 5. (Color online) Snapshots of the growing two-component system with A and B particles at a substrate temperature of 1,023 K and a deposition rate of 70 nm/h. The A and B particles are shown in yellow and red, respectively. The volume fraction of B particles is 3.0 vol%. (a) - (d) are the bird's-eye views and (a') - (d') are cross-sectional views corresponding to (a) - (d), respectively.

Fig. 6. (Color online) Number density of nanorods as a function of substrate temperature.

The simulations are performed at a deposition rate of 70 nm/h and a *B* particle volume fraction of 3.0 vol%.   The experimental data that correspond to BaHfO$_3$-doped SmBCO films are taken from our previous reports[10,12-14].   The experimental films were prepared by PLD method on LaAlO$_3$ single crystalline substrates and the BHO volume fractions were 3 - 4 vol%.   The bond energies were determined at 1,213 K as described in Sect. 2.   We plotted the simulated number density at 1,213 K as reference by a red cross point.

Fig. 7. (Color online) Bird's-eye views of *B* particle self-organization in the matrix consisting of *A* particles at a substrate temperature of 993 K.   Deposition rates of (a) 10, (b) 100, and (c) 1,000 nm/h.   Here, *A* particles are shown transparent for ease of viewing.   The volume fraction of *B* particles is 3.0 vol%.

Fig. 8. (Color online) Substrate temperature and deposition rate dependences of nanorods number density and nanostructures, which are the results of 3D-MC simulation.   (a) Contour plot of nanorod number density and (b) the phase diagram of nanostructures such as straight nanorods (NRs), inclined NRs, combination of short NRs and nanoparticles (NPs) and NPs.   The volume fraction of *B* particles is 3.0 vol%.

Table I. Experimental number density of BaHfO₃ nanorods in about 3 vol% BHO-doped SmBa₂Cu₃O$_y$ films for different substrate temperatures. For comparison, simulated results in this study are also listed.

Substrate temperature (K)	Number density (μm^{-2})	Simulated number density (μm^{-2}) (this study)
993 [23]	3,100	3,125
1,023 [22, 23]	2,300	2,500
1,113 [21]	1,440	1,406
1,213 [19]	708	781

(a)

A particle

B particle

$3a$

a

a

a

a

a

desorption

adsorption

Substrate
(A particles)

a

a

diffusion

(b)

E

0

vapor

E_{desorb}

$-E_{\text{desorb}}$

$E_{\alpha\beta}$; $\alpha, \beta = A$ or B

α

β

$-E_{\alpha\beta}$

on terrace

$-2E_{\alpha\beta}$

at step

$-3E_{\alpha\beta}$

at kink

$-4E_{\alpha\beta}$

in step

$-5E_{\alpha\beta}$

in terrace

$-6E_{\alpha\beta}$

in solid

Fig. 1.   (Color Online)

(a)

BMO nanorod

20 nm

80 nm

80 nm

(b)

BMO nanorod

20 nm

80 nm

80 nm

Fig. 2.   (Color Online)

(a) 2.24 × 10⁹ steps

(a') 2.24 × 10⁹ steps

(b) 4.16 × 10⁹ steps

(b') 4.16 × 10⁹ steps

(c) 9.60 × 10⁹ steps

(c') 9.60 × 10⁹ steps

(d') 113 × 10⁹ steps

(d) 113 × 10⁹ steps

20 nm

20 nm   20 nm

16 nm
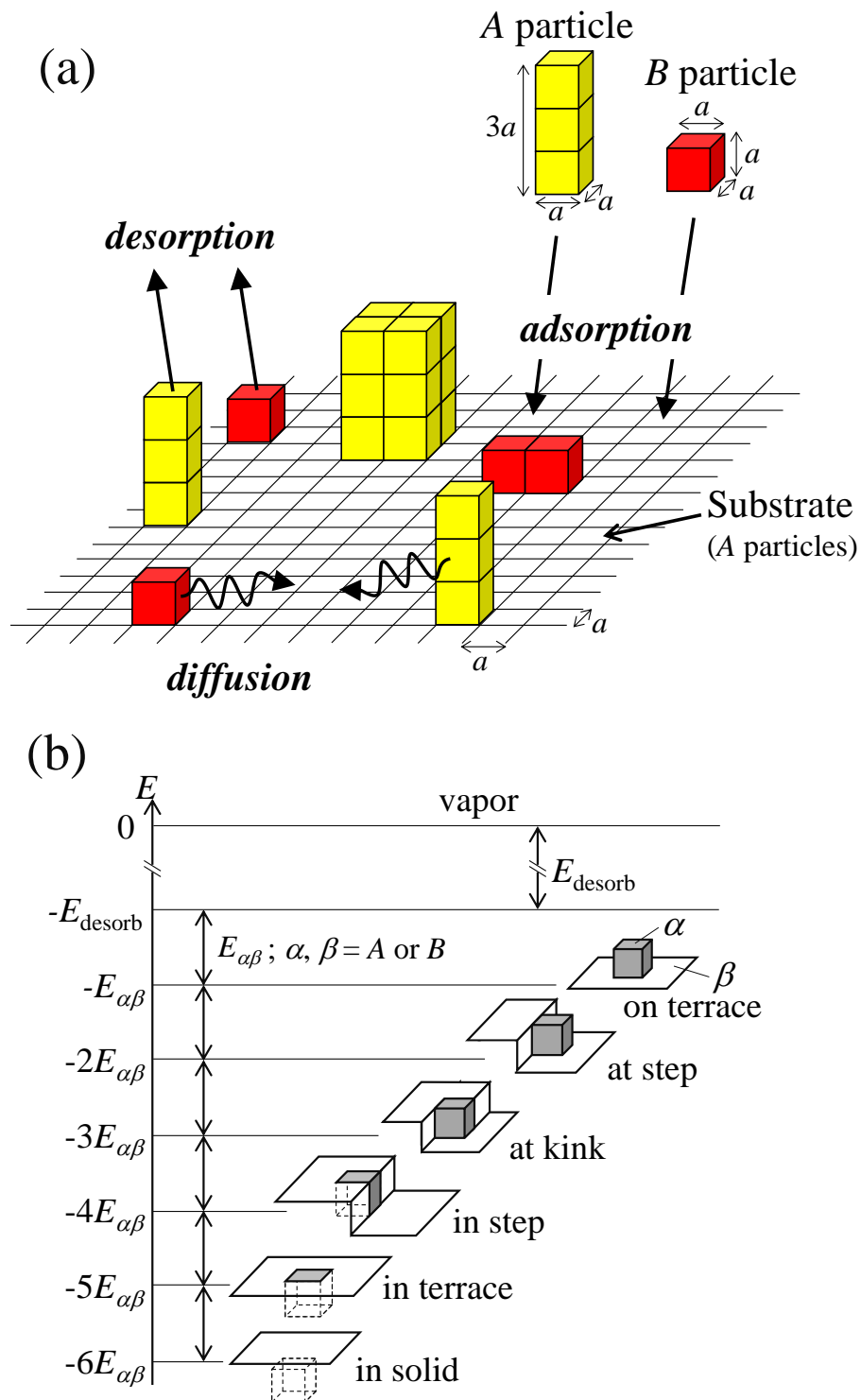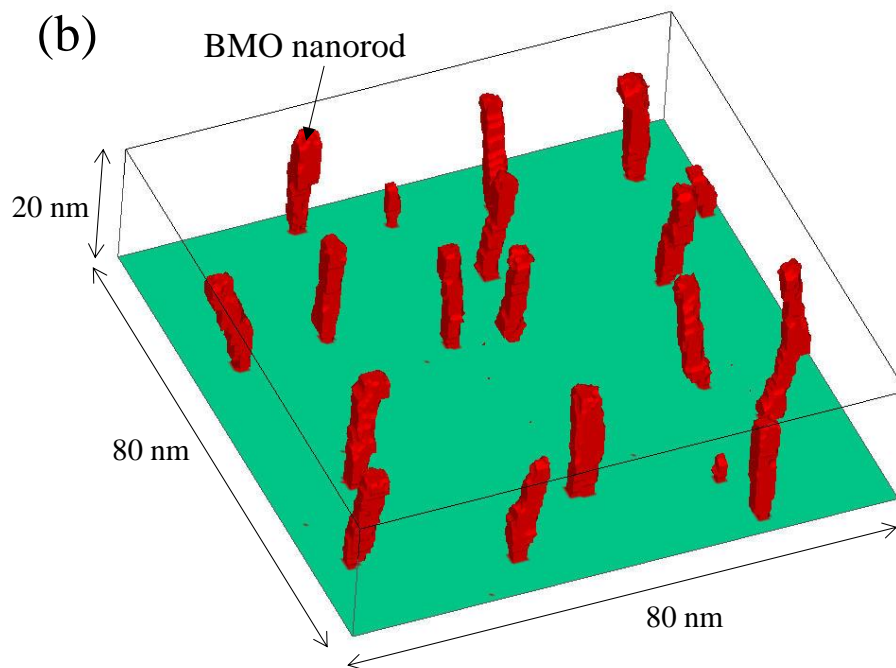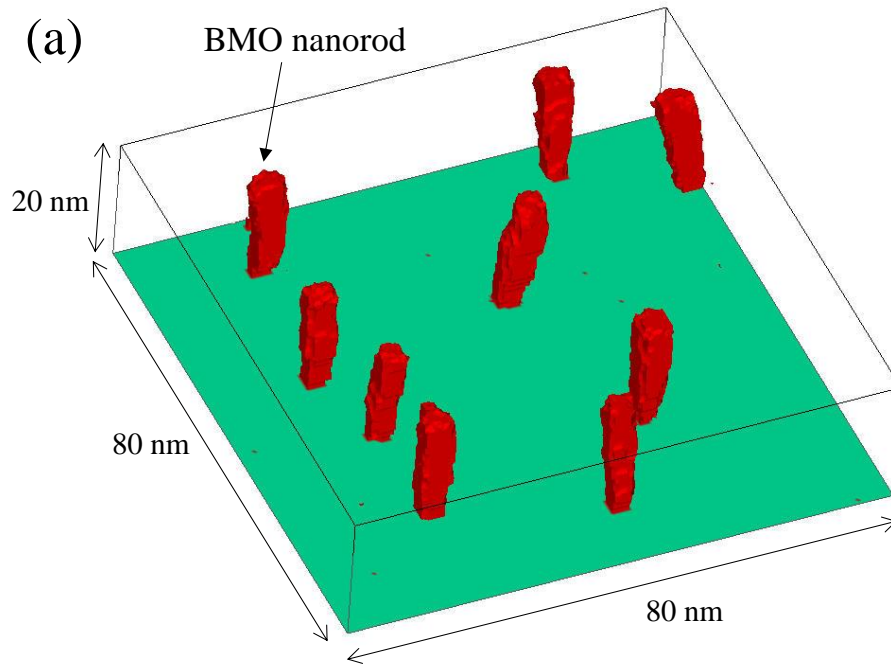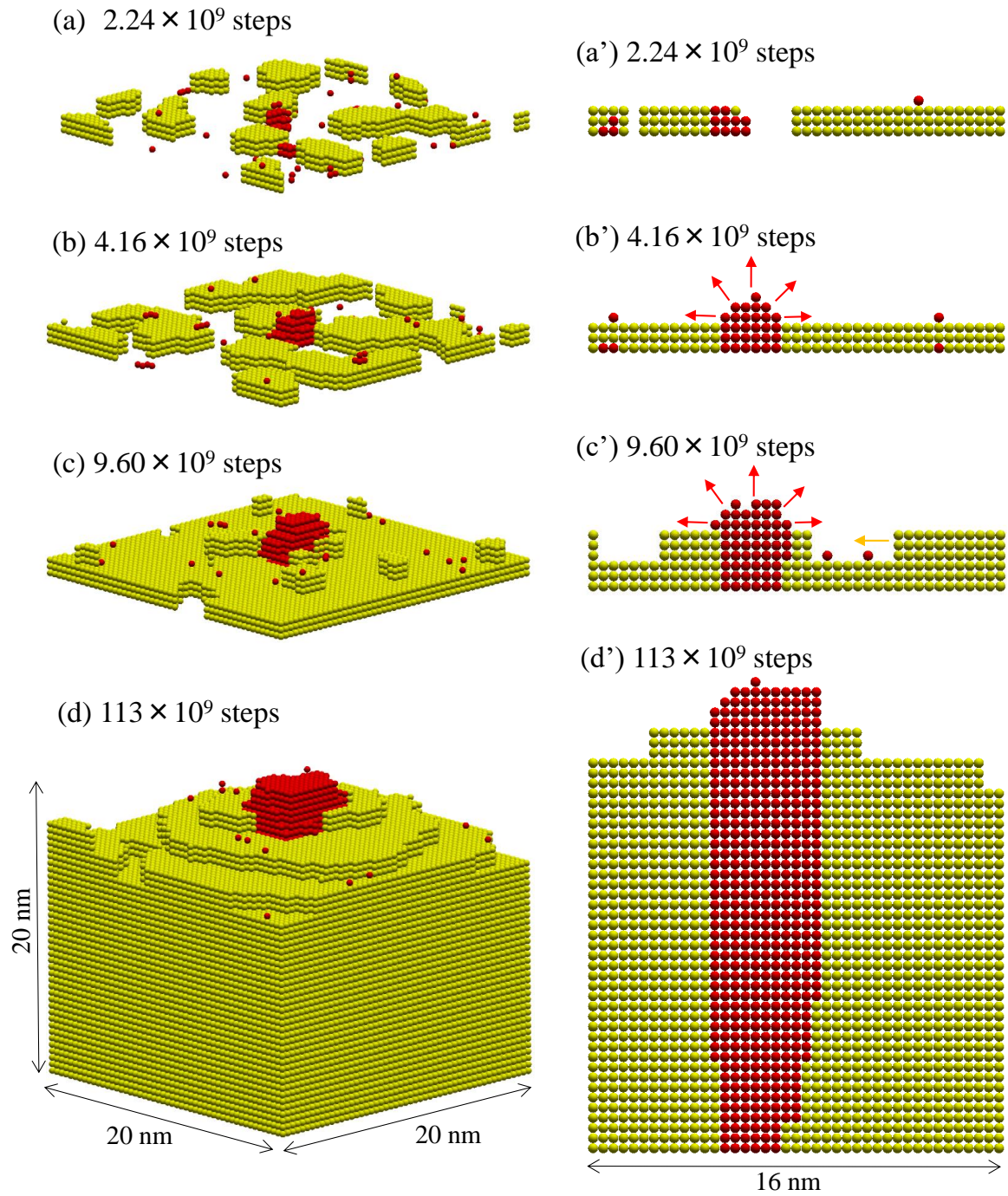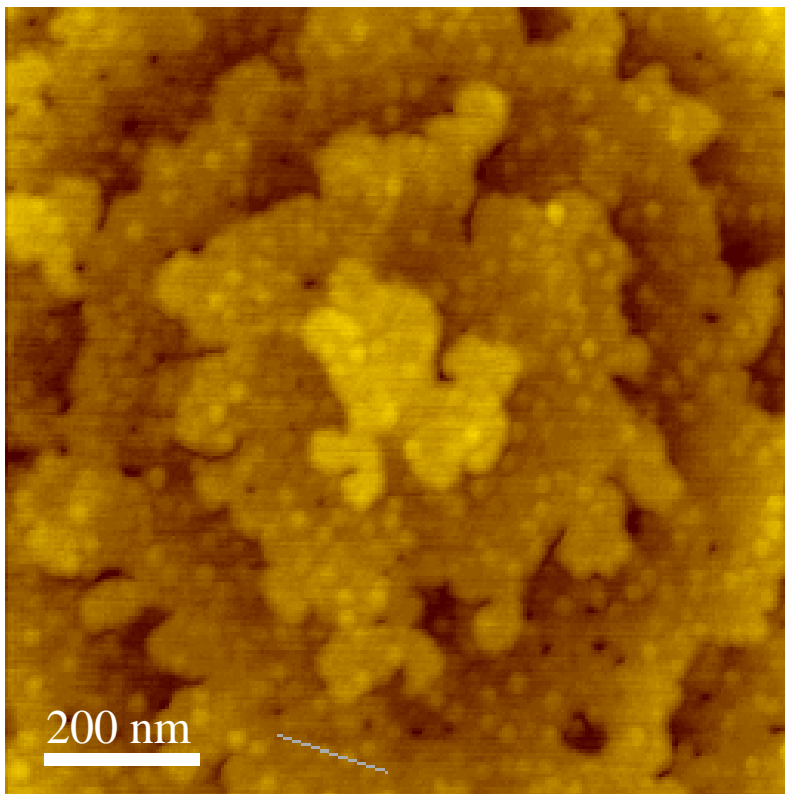
Fig. 3.   (Color Online)

Fig. 4.   (Color Online)

(a) 31.4×10^9 steps
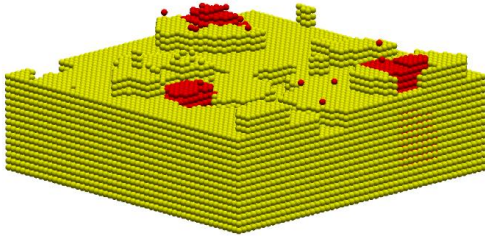
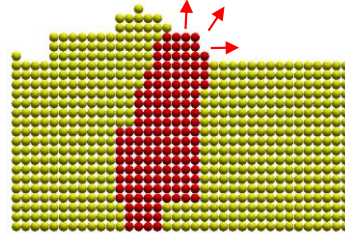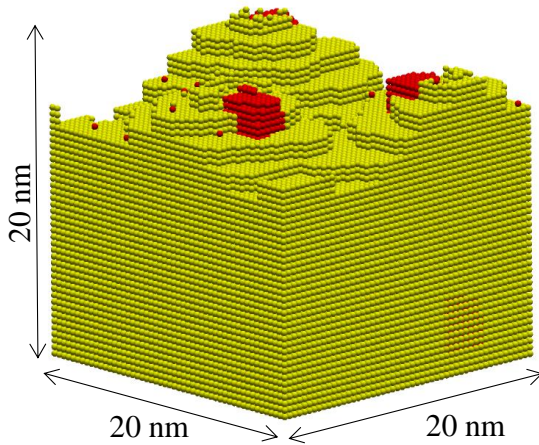(a') 31.4×10^9 steps
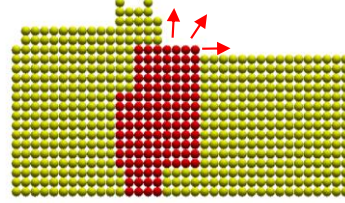
(b) 34.6×10^9 steps
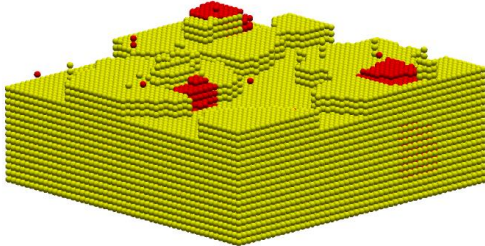
(b') 34.6×10^9 steps
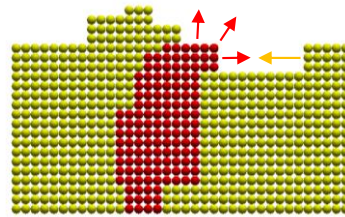
(c) 37.8×10^9 steps
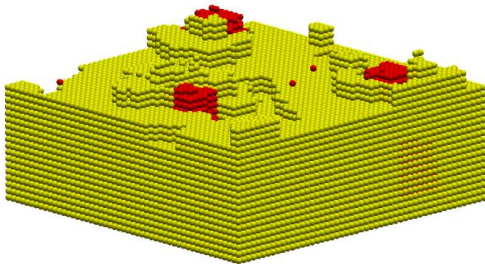
(c') 37.8×10^9 steps

(d) 79.7×10^9 steps
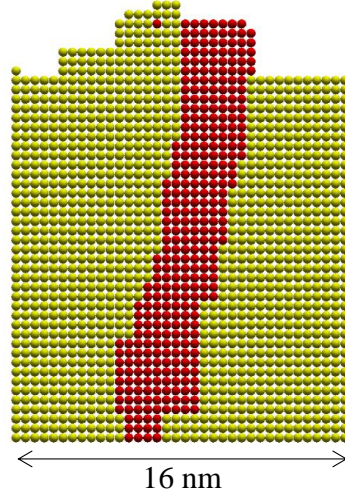
(d') 79.7×10^9 steps

20 nm

20 nm

20 nm
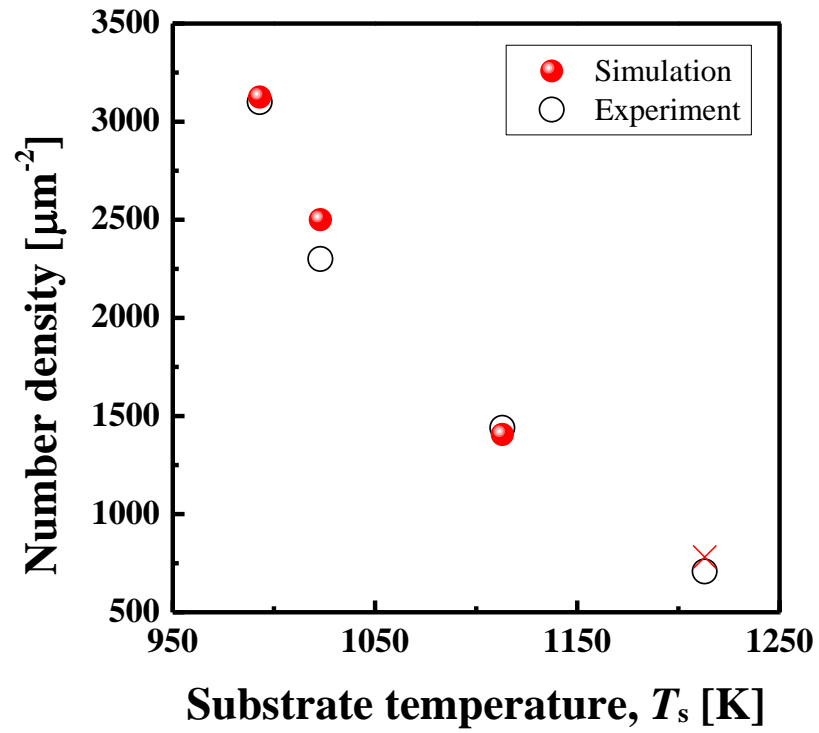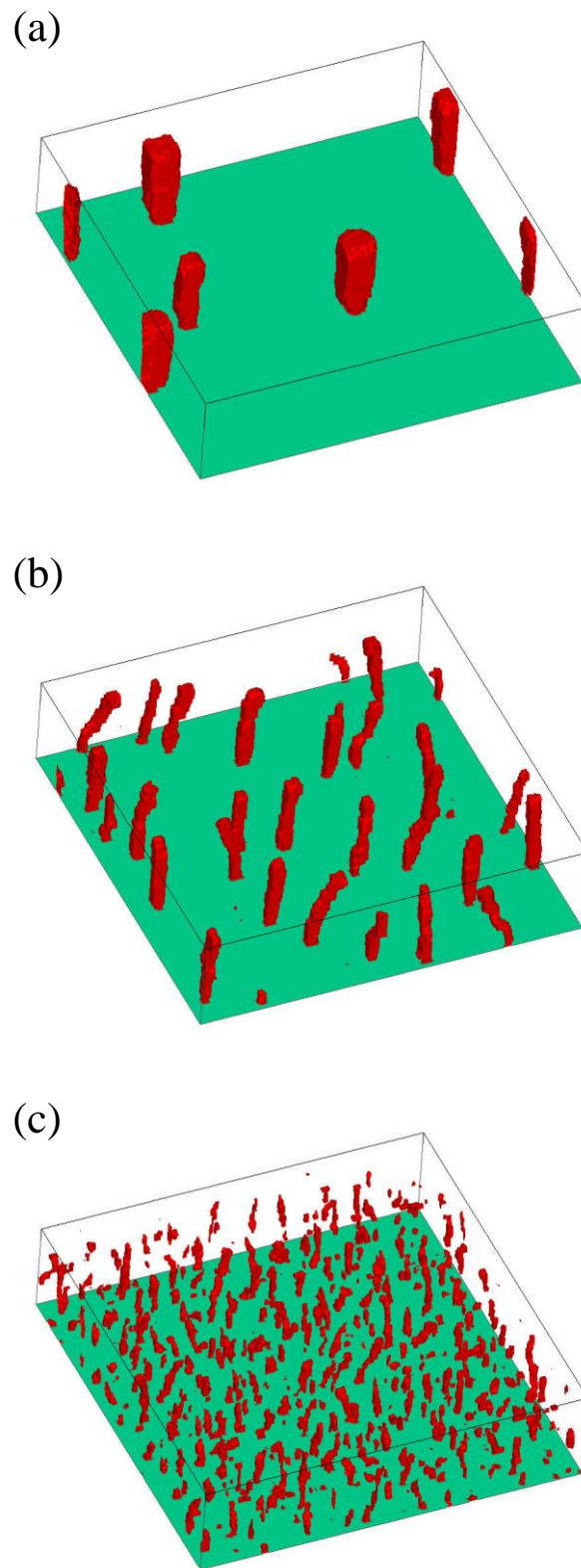
16 nm

Fig. 5.   (Color Online)

23

Fig. 6.   (Color Online)

(a)

(b)

(c)

Fig. 7.   (Color Online)

25

(a)

(b)

○ Straight NRs
△ Inclined NRs
□ Short NRs+ NPs
× NPs

Fig. 8. (Color Online)

26